

First-principles kinetic theory of precipitate evolution in Al-Zn alloys

This content has been downloaded from IOPscience. Please scroll down to see the full text.

2002 Modelling Simul. Mater. Sci. Eng. 10 131

(<http://iopscience.iop.org/0965-0393/10/2/303>)

View [the table of contents for this issue](#), or go to the [journal homepage](#) for more

Download details:

IP Address: 128.138.65.115

This content was downloaded on 14/07/2015 at 22:06

Please note that [terms and conditions apply](#).

First-principles kinetic theory of precipitate evolution in Al–Zn alloys

S Müller^{1,3}, L-W Wang² and Alex Zunger¹

¹ National Renewable Energy Laboratory, Golden, CO 80401, USA

² Lawrence Berkeley National Laboratory, Berkeley, CA 94720, USA

E-mail: s.mueller@fkp.physik.uni-erlangen.de

Received 20 November 2001

Published 9 January 2002

Online at stacks.iop.org/MSMSE/10/131

Abstract

The time evolution of the distribution of precipitate shapes and sizes in Al–Zn alloys is studied via a mixed-space cluster expansion and kinetic Monte-Carlo simulations. We find that the growth of precipitates in Al-rich Al–Zn alloys follows classical Ostwald ripening already after ageing times of a few seconds. Moreover, the distribution of the precipitates is temperature-dependent: the higher the ageing temperature, the smaller the distribution width of the precipitate size. We discuss the time evolution of the precipitates in terms of short-range order parameters and compare them with experimental data.

1. Introduction

Quenching a solid solution of a binary metal alloy into the two-phase region of the phase diagram (shown in figure 1 for the system Al–Zn [2,3]) leads to the formation of characteristic precipitate microstructures [1]. Of special importance are *coherent* precipitates that have no dislocations between the precipitate and the matrix. In heat-treatable light-metal alloys [4] such as Al–Cu, Al–Mg, and Al–Zn, coherent precipitates effectively impede dislocation motion [1,4–6]. The chemical and structural properties of such precipitates are determined by the identity of the phases being located to the left and right of the two-phase region in the phase diagram (figure 1). In the case of the phase-separating system Al–Zn, the two-phase region corresponds to elemental Al and Zn, so that precipitates formed from the Al-rich solid solution consist of only Zn atoms. Our previous Monte-Carlo (MC) simulations of precipitates in Al–Zn [7] have shown that although the precipitates are created by an inherently kinetic heat treatment process, the *size versus shape relation* of fully developed precipitates ($t \rightarrow \infty$) can be explained in terms of *thermodynamic* arguments [7,8]. However, the *distribution* of precipitate shapes and sizes at finite ageing time is controlled by *kinetics*. Here, we study the kinetic evolution of these precipitates. The kinetic evolution of an alloy morphology is important for understanding how the final shape of the alloy comes about.

³ Permanent address: University Erlangen–Nürnberg, Lehrstuhl für Festkörperphysik, Staudtstrasse 7, 91058 Erlangen, Germany.

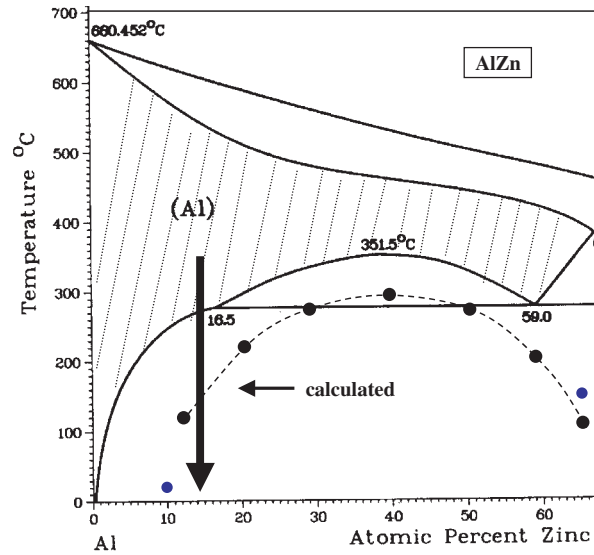


Figure 1. Al-rich side of the Al–Zn phase diagram. The dashed curve gives our calculated fcc miscibility gap [2]. Quenching a solid solution below this line leads to the formation of coherent precipitates. The experimental phase diagram was taken from [3].

The kinetic MC method [9–11] is one of the most successful approaches to describe diffusion, growth, and microstructure evolution in alloy systems [12]. Various approaches for describing shape evolution of microstructures in alloys use different methods such as the Onsager equation in mean-field approximation [13–15], a microscopic mean-field kinetic equation [16], the stochastic field method [17], or the discrete atom method [18–20]. In contrast to such continuum models that require a knowledge of the energy surface for *arbitrary atomic configurations*, we use an atomistic method [21] which requires only the energies $E(\sigma)$ of *substitutional configurations* σ . The latter energies can easily be calculated within the local density approximation (LDA) [22, 23] fitted to a generalized Ising cluster expansion $E_{\text{CE}}(\sigma)$. One can use $E_{\text{CE}}(\sigma)$ in conventional (not kinetic) MC simulations to study the *thermodynamic* properties of the system. This approach was previously applied to describe the size versus shape relation of coherent precipitates in Al–Cu [24], Al–Mg [25], and Al–Zn [7, 8]. For the latter system, we found, in excellent agreement with experimental data (see [7] and references therein), that with increasing size and decreasing temperature the shape of an individual precipitate changes from a more spherical/compact shape to a more ellipsoidal/plate-like shape. We have also calculated the coherent phase boundary, i.e. the locus of composition–temperature points at which solubility in the solid solution phase is lost and coherent precipitates are formed. We have calculated this line from MC simulations of $E_{\text{CE}}(\sigma)$ [2] leading to a maximum at $T_c = 295^\circ\text{C}$ in the phase diagram for $x_{\text{Zn}} = 0.40$ (figure 1), in excellent agreement with experimental values (see the references given in [2]).

In this paper, we apply *kinetic MC* simulations to the alloy system Al–Zn investigating the time evolution of the final morphology. Experimental studies of kinetic properties of precipitates in Al–Zn reveal the following behaviour [26, 27]: (i) The distribution of precipitate shapes changes with ageing time: the longer the ageing time, the less spherical and the more ellipsoidal the precipitates become. (ii) The width of the distribution of precipitate shapes and sizes depends on the heat treatment. Lowering the ageing temperature leads to a broadening of

the size distribution compared with higher ageing temperatures. (iii) After the initial formation of precipitates within the first few seconds for a given temperature and concentration, the short-range order parameters of the alloy only show a weak time dependence. In the following, we show that it is possible to predict, describe, and understand these effects via an atomistic, first-principles LDA-based cluster expansion [21]. Using our theoretical model, we will study, as a function of ageing time, (i) the distribution of Zn clusters at different temperatures, (ii) the number of precipitates, and (iii) the time evolution of the short-range order of the alloy. We will compare our results with those expected from classical Ostwald ripening which would predict a $t^{1/3}$ evolution for the average precipitate diameter.

2. Method

2.1. Cluster expansion of substitutional configurational energies

The energy $E_{\text{CE}}(\sigma)$ of substitutional configurations is given by a mixed-space cluster expansion (MSCE) [21]. In this approach, any configuration σ is defined by specifying the occupations of each of the N lattice sites by an Al atom (spin index $\hat{S}_i = -1$) or a Zn atom ($\hat{S}_i = +1$). The formation enthalpy of any substitutional configuration σ at its atomically relaxed state is then given by

$$\Delta H_{\text{CE}}(\sigma) = \sum_{\mathbf{k}} J_{\text{pair}}(\mathbf{k}) |S(\mathbf{k}, \sigma)|^2 + \sum_f^{\text{MB}} D_f J_f \bar{\Pi}_f(\sigma) + \frac{1}{4x-1} \sum_{\mathbf{k}} \Delta E_{\text{CS}}^{\text{eq}}(\hat{k}, x) |S(\mathbf{k}, \sigma)|^2. \quad (1)$$

The first sum describes all possible pair figures. It is expressed in reciprocal space, thus affording a converged description of even long-range pair interactions [28]. Here, $J_{\text{pair}}(\mathbf{k})$ is the lattice Fourier transform of the real-space pair interactions, and $S(\mathbf{k}, \sigma)$ are structure factors. The second sum describes many-body (MB) figures, such as triangles, tetrahedra, etc. Here, J_f is the real-space many-body interaction of figure f , D_f stands for the number of equivalent clusters per lattice site, and $\bar{\Pi}_f(\sigma)$ are spin products. The last term in equation (1) describes the constituent strain energy necessary to maintain coherency between bulk Al and fcc Zn along an interface with orientation \hat{k} . It can be calculated by deforming the bulk elements (Al and fcc Zn) from their equilibrium lattice constants a_{Al} and a_{Zn} to a common lattice constant a perpendicular to \hat{k} . We see that the first two terms in equation (1) describe *atomistically* the ‘chemical energy’ of a configuration, while the third term describes the anisotropic (and generally anharmonic) long-range strain energies.

We determine $\{J_{\text{pair}}(\mathbf{k})\}$ and $\{J_f\}$ by fitting $\Delta H_{\text{CE}}(\sigma_{\text{ord}})$ to a set of corresponding enthalpies $\Delta H_{\text{LDA}}(\sigma_{\text{ord}})$ of 26 ordered (ord) Al_nZn_m compounds. The sets $\{\sigma_{\text{ord}}\}$ include (among others) superlattices of different Zn compositions $x = 0, 0.125, 0.25, 0.33, 0.40, 0.50, 0.60, 0.66, 0.75, 1.0$ and layer orientations (001), (110), (111), (201), (311). These formation enthalpies are calculated within the LDA as implemented by the pseudopotential plane-wave method [29]. Comparing ΔH_{CE} with ΔH_{LDA} for nine ordered Al–Zn compounds which were not used in the construction of $\{J_{\text{pair}}(\mathbf{k})\}$ and $\{J_f\}$ shows an average prediction error of only 2 meV/atom [2]. This accuracy requires inclusion of up to 20 pair interactions.

2.2. Kinetic MC algorithms

Our kinetic algorithms use very simple approximations: (i) The precipitates are formed by site-flips only and not by continuous atomic motions. The energies $E_{\text{CE}}(\sigma)$ before and after

spin-flips always correspond to geometrically fully relaxed configurations. This is guaranteed by our MSCE-Hamiltonian of equation (1). (ii) Our model does not have vacancies. (iii) In order to consider the energy barriers between different configurations, we accept information from experiment: our jump frequencies, $1/\tau_0$, as a function of temperature T were taken from the experimental diffusion constant $D_{\text{exp}}(T)$ via

$$\tau_0(T) = \frac{a_{\text{nn}}^2}{D_{\text{exp}}(T)}, \quad (2)$$

where a_{nn} is the average nearest-neighbour distance between atoms. The experimental determined function $D_{\text{exp}}(T)$ was taken from Hatch [4]. It is possible, however, to compute diffusion coefficients from first-principles, but this will not be done here. Although this seems to be a very rough approximation, $D_{\text{exp}}(T)$ contains a real ‘average’ energy barrier and, therefore, our jump frequency implicitly contains this information too. We will see that this simple approximation leads to very reasonable results regarding the time evolution of the precipitate size distribution. It should be noted that this approximation pertains only to the activation barrier and *not* the configurational energy, $E(\sigma)$, given by the MSCE of equation (1).

We constructed two types of algorithm, which we will call ‘algorithm I’ and ‘algorithm II’. Algorithm I (described here for Al-rich Al–Zn alloys) has the following simple structure:

1. Find all of the N Zn atoms in a random configuration, order them by site indices, and choose the first Zn atom.
2. Determine how many of its neighbours are Al atoms.
3. Select randomly one of the Al neighbours.
4. If the energy difference δE caused by flipping the two atoms is $\delta E < 0$, flip the two spins, but if $\delta E > 0$, flip the two spins with a probability of $\exp(-\delta E/kT)$. Here, E is obtained from equation (1). Note that this energy corresponds to the case where all atoms are relaxed to the (local) minimum of energy at the configuration σ .
5. Repeat steps 2–4 for all Zn atoms.
6. Use equation (2) to transfer 1 MCS into ‘real time’.
7. Go to 1.

In this algorithm, one Monte-Carlo step (MCS) is defined as ‘one trial to jump for each Zn atom’. The *advantages* of this algorithm are: (i) Zn atoms are not chosen randomly, but each Zn atom has the chance to jump once per time step. Therefore, the jumps of different Zn atoms are as simultaneous as possible. (ii) One MCS represents a constant time interval which allows a very simple transformation in real time. The *disadvantage* of this algorithm is that it becomes inefficient when most of the Zn atoms are already attached to only a few large precipitates. Then, the jump probabilities become very low (especially for low temperatures), because Al–Zn possesses clustering tendencies. Zn atoms that are in the interface region between Zn precipitate and Al matrix will practically never leave the surface of the Zn precipitate. We find that in the case of Al–Zn, algorithm I works best for temperatures $T \geq 200$ K and ageing times $t \leq 15$ min.

An ansatz for a possible solution of this problem could be (a) try cluster algorithms and (b) force an atom to move. Cluster algorithms (see e.g. [30, 31]) are based on the idea that forming a cluster consisting of many spins first and flipping them simultaneously is less time consuming than flipping individual spins. However, such algorithms are not very efficient if the formation of large clusters is very time consuming by itself, but the probability for flipping them is very low. In this case, for many formed clusters their flip is rejected. This is exactly the situation encountered in phase-separating systems like Al–Zn.

The main problem of forcing a Zn atom to leave a precipitate surface (method (b)) is that this Zn atom will most likely return to the precipitate surface in the next MCS. If we

forbid this second step in the simulation, we would be confronted with a non-Markovian process demanding a complex reconsideration of the function between experimental diffusion constant and the computer time unit ‘MCS’. Furthermore, the following question arises: for how many MCSs the ‘returning’ event has to be forbidden. Even if we do not allow for a certain Zn atom to jump back to the precipitate surface in MCS number j , from which it was removed in MCS number $j - 1$, it is very likely that this ‘returning’ event will happen in MCS number $j + 1$. The best solution for the above problem seems to be an algorithm where the chosen Zn atom is forced to jump *without destroying the Markovian process*. This is realized in the following algorithm—algorithm II:

1. Find all of the N Zn atoms in a random configuration and order them by site indices.
2. Determine all the possible jumps S for each of the N Zn atoms (for an fcc lattice $S^{\max} = 12N$, if all Zn atoms would only have Al atoms as neighbours).
3. Calculate the energy change $\delta E(i)$ for each allowed jump for all Zn atoms ($i = 1, \dots, S$).
4. If $\delta E(i) > 0$, calculate $W_i = (1/\tau_0) \exp(-\delta E(i)/kT)$. If $\delta E(i) < 0$, calculate $W_i = 1/\tau_0$.
5. Calculate $P_i = W_i / W_{\text{tot}}$, where $W_{\text{tot}} = \sum_{i=1}^S W_i$.
6. Select randomly one jump i from the S possible events according to their probability P_i .
7. Calculate the new total simulation time $t_{\text{MCS}} = t_{\text{MCS}-1} + 1/W_{\text{tot}}$. (Note that $W_{\text{tot}} = \sum_{i=1}^S W_i$ is *not* a constant, but is different for each MCS. So, recording t_{MCS} after each MCS is a ‘must’.)
8. Recalculate all $\delta E(i)$ ’s.
9. Go back to step 4.

The efficiency of this method strongly depends on the question of whether the calculation of the new $\delta E(i)$ ’s (step 8) is time intensive. An accepted spin-flip demands a recalculation of $S(\mathbf{k}, \sigma)$ in equation (1). However, as shown by Lu *et al* [32], the MSCE method allows one to avoid the necessity of recalculating $S(\mathbf{k}, \sigma)$ after each move by directly calculating the *change* in $J_{\text{pair}}(\mathbf{k})|S(\mathbf{k}, \sigma)|^2$ for each move in real space [32]. In practice, algorithm II is clearly slower for short ageing times and high temperatures, i.e. where nearly every flip is accepted. The advantage of algorithm II lies in the simulation of long ageing times. As we can see from step 4 of the algorithm description, now a single MCS is *no longer a constant real time unit*, but depends on the corresponding probability W_{tot} . In practice, one MCS can now represent real times of 1/1000 s up to many minutes. As a rough rule, we can conclude that algorithm II is to be preferred, if one MCS corresponds to a real time of about 1 s.

It should be mentioned that in algorithm II a single MCS corresponds indeed to only one flip of one Zn atom and *not* one trial-flip of each Zn atom. Since flip channel i is always chosen randomly and we mostly consider a large number of Zn atoms (e.g. 1000–15 000), the probability that the same Zn atom is chosen in MCS i , when it was already chosen in MCS $i - 1$, is very small. So, due to the large system size, it is not necessary to forbid any kind of jumps between Al and Zn atoms, i.e. we do not have to give up the restriction that the algorithm should be based on the Markovian process. The concept of algorithm II is very similar to that of the so-called ‘residence-time algorithm’ [11], where also one transition is performed at each MCS. Different from the work of Soisson *et al* [33], who applied such an algorithm to study Cu precipitation in Fe–Cu alloys, our model does not consider any vacancy jump mechanism. Also, in our calculation the configurational part of the energy is treated with LDA accuracy. Our present kinetic simulations are restricted to nearest-neighbour jumps only. This is not generally justified, although it was already successfully applied in the literature (see e.g. [18]). For certain applications, a necessary extension to second, third, and further neighbour jumps may be needed.

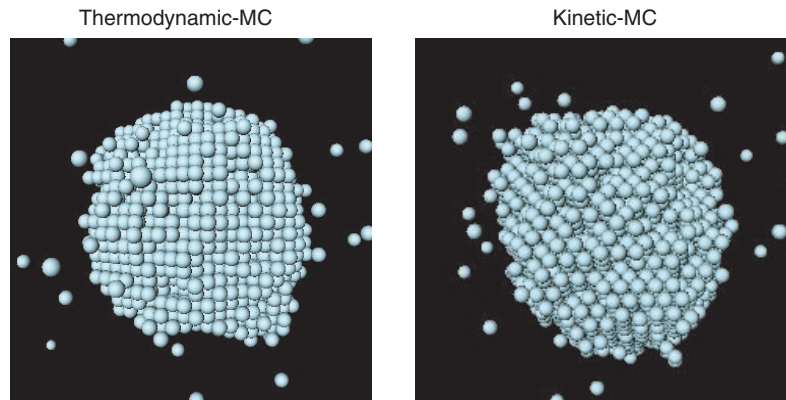


Figure 2. Comparison between equilibrium configurations for an $\text{Al}_{0.92}\text{Zn}_{0.08}$ alloy resulting from thermodynamic and kinetic MC simulations (only Zn atoms are shown).

Both algorithms fulfil the condition of detailed balance. Although the kinetic MC algorithms are not efficient for studying equilibrium configurations (since they are much slower than a simple thermodynamic MC algorithm), for higher temperatures it is still possible and, therefore, a reasonable test to check if the kinetic MC code leads within statistical accuracy to the same equilibrium configurations obtained by standard equilibrium MC. The code we used for studying thermodynamic properties is a simple Metropolis algorithm allowing for flipping of pairs of Al and Zn atoms in *arbitrary* distance (i.e. does not simulate a realistic kinetic process) in order to reach the equilibrium configuration as fast as possible:

1. Select randomly one Zn and one Al atom.
2. Calculate the energy difference δE caused by flipping the two atoms. If $\delta E < 0$, flip the two spins, but if $\delta E > 0$, flip the two spins with a probability of $\exp(-\delta E/kT)$ (again, E is obtained from equation (1)).
3. Go to 1.

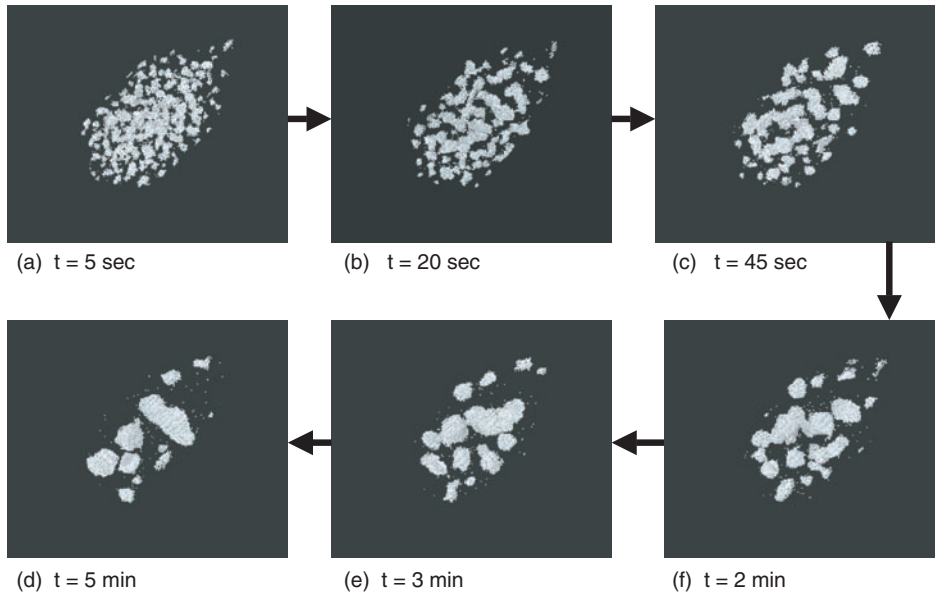
We made such tests for a number of different MC cells and concentrations. As an example for the kinetic MC versus thermodynamic MC comparison, figure 2 shows the result for an $\text{Al}_{0.92}\text{Zn}_{0.08}$ alloy, embedded in a $30 \times 30 \times 30$ MC cell at $T = 300$ K (only Zn atoms are shown). For $x_{\text{Zn}} = 0.08$ the chosen temperature of 300 K is below the coherent miscibility line (figure 1), so a precipitate should occur. The agreement between the predicted precipitate shape in kinetic MC and thermodynamic MC seen in figure 2 is very good. It should be mentioned that the computer time needed for reaching the equilibrium configuration is about a factor of 30 longer for the kinetic than for the thermodynamic MC algorithm. For a more quantitative comparison, table 1 gives the first ten Warren–Cowley short-range order parameters α_{lmn} (for the definition of α_{lmn} , see section 4) as obtained by the kinetic and equilibrium MC simulations. The agreement is excellent.

3. Precipitate growth and precipitate size distribution as a function of ageing time

We chose an $\text{Al}_{0.932}\text{Zn}_{0.068}$ alloy possessing a critical temperature of $T_c \approx 330$ K. The MC cell used consists of $56 \times 56 \times 56$ sites (total of 175 616 atoms) which contains a total of 11 942 Zn atoms. Figure 3 shows the time evolution of the precipitate configurations at $T = 250$ K.

Table 1. Calculated SRO parameters (equation (4)) of an $\text{Al}_{0.92}\text{Zn}_{0.08}$ alloy ($T = 300\text{ K}$) via kinetic and thermodynamic MC. The values correspond to the configurations shown in figure 2.

(lmn)	$\alpha_{lmn}^{\text{thermo}}$	$\alpha_{lmn}^{\text{kin}}$
000	1.000	1.000
110	0.704	0.700
200	0.646	0.628
211	0.615	0.601
220	0.590	0.586
310	0.568	0.566
222	0.536	0.519
321	0.527	0.511
400	0.519	0.503
330	0.499	0.477
411	0.502	0.478

**Figure 3.** Zn precipitates in Al–Zn as a function of ageing time. With increasing t , the average size of the precipitates increases while their number decreases (only Zn atoms are shown).

We see that (i) already after 5 s, small Zn precipitates are visible with less than 10% of the Zn atoms remaining in solution, and (ii) with increasing ageing time, the number of precipitates decreases while their average size increases. Indeed, the number of precipitates decreases from $N_p = 58$ at $t = 5\text{ s}$ down to $N_p = 10$ at $t = 5\text{ min}$.

In order to see the influence of the ageing temperature on the precipitate size distribution, figure 4 shows configurations for two different temperatures and ageing times. We see that, for a constant ageing time, (a) the number of precipitates is larger for the lower ageing temperature, and (b) the average size of precipitates is larger for the higher ageing temperature. In order to quantify these observations, figure 5 gives a logarithmic presentation of the number of precipitates N versus the ageing time t for three different temperatures. In all cases, the $\log N$ versus $\log t$ plot shows a slope close to -1 (given by the dashed line) being expected for

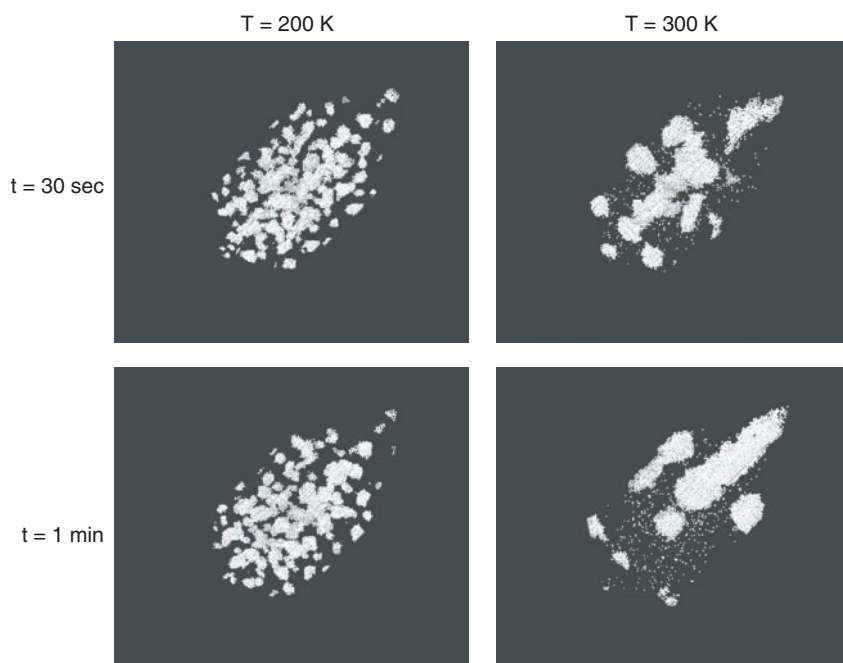


Figure 4. Zn precipitates in Al–Zn for two different ageing temperatures and times. For a constant ageing time, a higher ageing temperature leads to larger, but less, precipitates (only Zn atoms are shown).

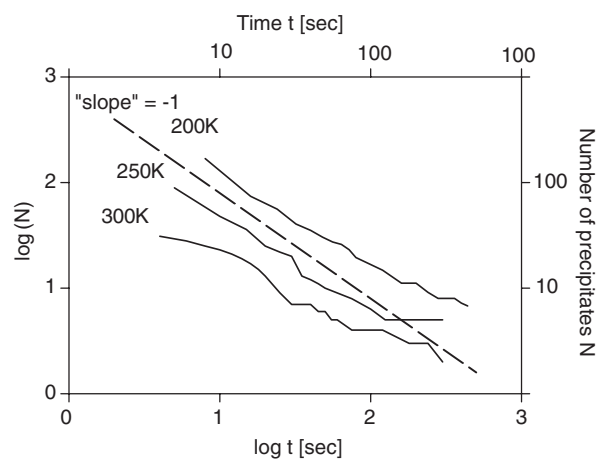


Figure 5. Logarithmic plot of number of precipitates versus ageing time in an $\text{Al}_{0.932}\text{Zn}_{0.068}$ alloy (11 942 Zn atoms) for three different temperatures. The slope of all three curves is very close to -1 , i.e. the expected value for classical Ostwald ripening (---).

classical Ostwald ripening. The fluctuations within each individual curve come by the limited system size. So, e.g. for an ageing temperature of 250 K and an ageing time of 5 min, there are only ten precipitates left leading to quite poor statistics. Figure 6 displays the ‘mean diameter’, d_m , of all precipitates as a function of ageing time for $T = 250$ K. Here, d_m represents the diameter of the corresponding sphere having the same volume as the observed precipitate.

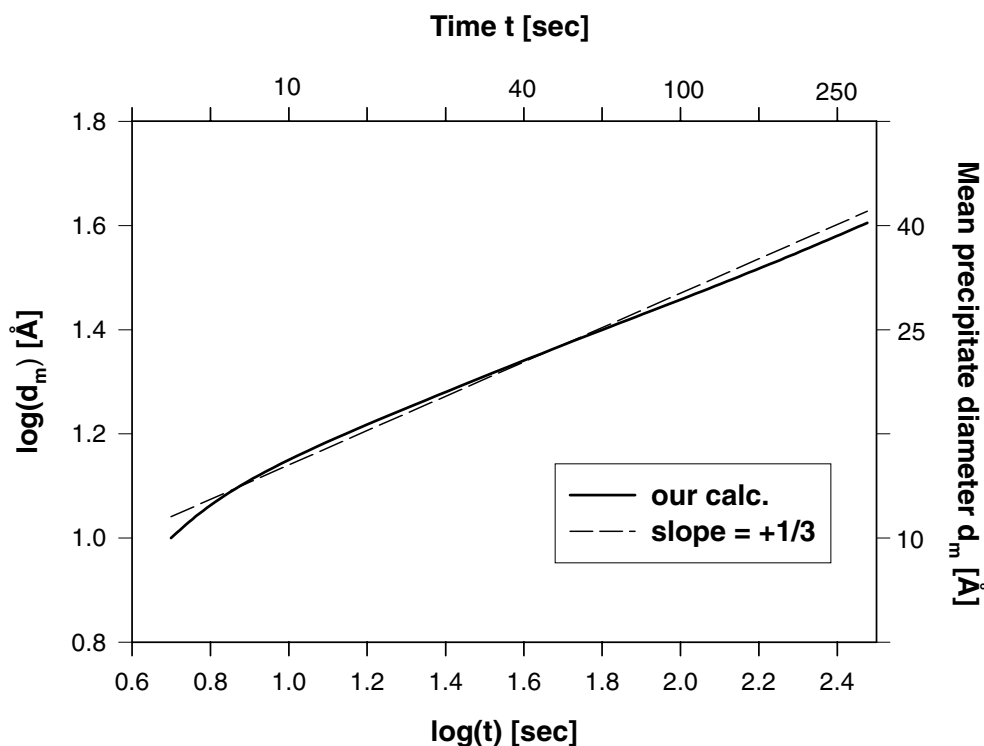


Figure 6. Logarithmic plot of mean precipitates diameter d_m as a function of ageing time. The resulting curve shows a slope of 0.31 very close to $1/3$ (---) expected for Ostwald ripening.

It is given by $d_m = 2r_m = 2(ca^2)^{1/3}$, where c and a are the thickness and length of the ellipsoidal precipitates, respectively. Again, a logarithmic presentation is used allowing for a direct determination of the observed slope. We find a slope of 0.31 very close to the $1/3$ slope of classical Ostwald ripening (given by the dashed line in figure 6). So, our result suggests that the *growth process* of precipitates in Al–Zn represents an example of Ostwald ripening: smaller precipitates disappear with increasing ageing time, while larger precipitates appear leading to an increase of the mean diameter d_m via $d_m \propto t^{1/3}$.

Following figure 6, there is however a clear deviation from the $t^{1/3}$ kinetics within the first few seconds ($t \leq 5$ s) of ageing time, i.e. when the precipitates are formed. It is very likely that initial composition fluctuations play an important role in the formation of the ‘seeds’ of precipitation leading to a two-stage model. A detailed study of this nucleation process demands future effort. In the framework of this paper, we concentrate on the ripening process of the precipitates.

Figure 7 shows a distribution of precipitate sizes as a function of ageing time. In this bar chart presentation, precipitates are defined again by their average mean diameter given by $d_m = 2r_m = 2(ca^2)^{1/3}$. We see that: (i) For very short ageing times ($t = 10$ s), most of the precipitates are extremely small ($d_m < 15$ Å) and, therefore, possess a very compact shape. (ii) With increasing ageing time, the average precipitate size increases (note that the scale of the y-axis (number of precipitates) is different for the different ageing times). Unfortunately, for $t = 5$ min our statistics are already pretty poor, because there are only ten precipitates left. However, the tendency to get larger precipitates with increasing ageing time is still visible.

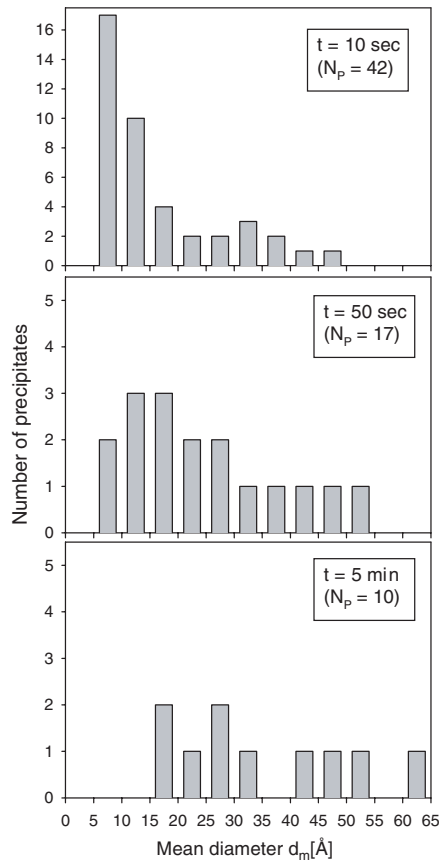


Figure 7. Distribution of precipitates for three different ageing times ($T = 250$ K).

Figure 8 shows the distribution of precipitates as a function of temperature. An ageing time of $t = 30$ s was chosen for the comparison. We see that (i) the maximum in the distribution shifts to higher d_m values with increasing ageing temperature, and (ii) lower ageing temperatures lead to a broadening of the size distribution. Thereby, the size distribution width, Δd_m , is 55, 40, and 35 Å for temperatures of 200, 250, and 300 K, respectively (again, statistics are quite poor for $T = 300$ K, because there are only eight precipitates left). This tendency agrees with experimental investigations by Ramlau and Löffler [26] using the same Zn concentration as we did. Unfortunately, a quantitative comparison is not possible, since simulation of an ageing time of 19 days (used by the authors) would (a) most likely lead to the equilibrium configuration, i.e. a configuration consisting of one precipitate only caused by the limited system size in our simulation, and (b) lead to unreasonably long computer times of about several months.

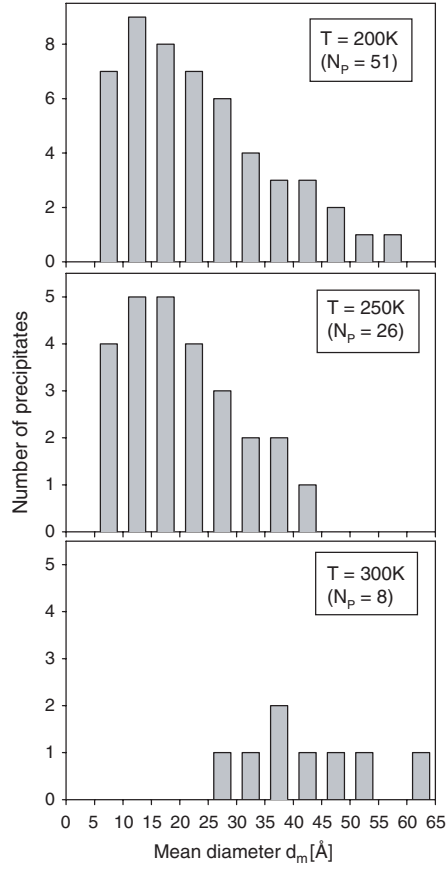


Figure 8. Distribution of precipitates for three different ageing temperatures ($t = 30$ s).

4. Dependence of SRO on ageing time and temperature

The short-range order (SRO) can be described in terms of the Warren–Cowley SRO parameters which are given for shell (lmn) by

$$\alpha_{lmn}(x) = 1 - \frac{P_{lmn}^{A(B)}}{x}, \quad (3)$$

where $P_{lmn}^{A(B)}$ is the conditional probability that, given an A atom at the origin, there is a B atom at (lmn). The sign of α indicates qualitatively whether atoms in a given shell prefer to order ($\alpha < 0$) or cluster ($\alpha > 0$). The SRO parameter may be written in terms of the pair correlations as

$$\alpha_{lmn}(x) = \frac{\langle \bar{\Pi}_{lmn} \rangle - q^2}{1 - q^2}, \quad (4)$$

where $q = 2x - 1$ and $\langle \bar{\Pi}_{lmn} \rangle$ is the pair correlation function for shell (lmn). In diffraction experiments, the portion of diffuse scattering due to SRO is proportional to the lattice Fourier transform of $\alpha_{lmn}(x)$:

$$\alpha(x, \mathbf{k}) = \sum_{lmn}^{n_R} \alpha_{lmn}(x) e^{i \cdot \mathbf{k} \cdot \mathbf{R}_{lmn}}. \quad (5)$$

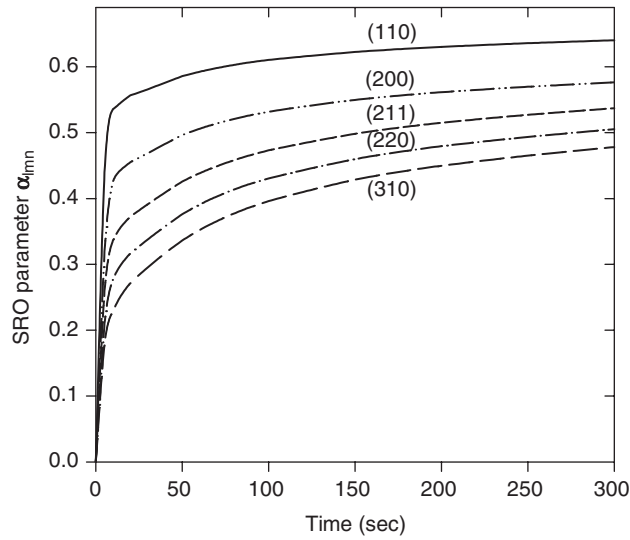


Figure 9. Time dependence of the first five Warren-Cowley SRO parameters ($T = 250$ K).

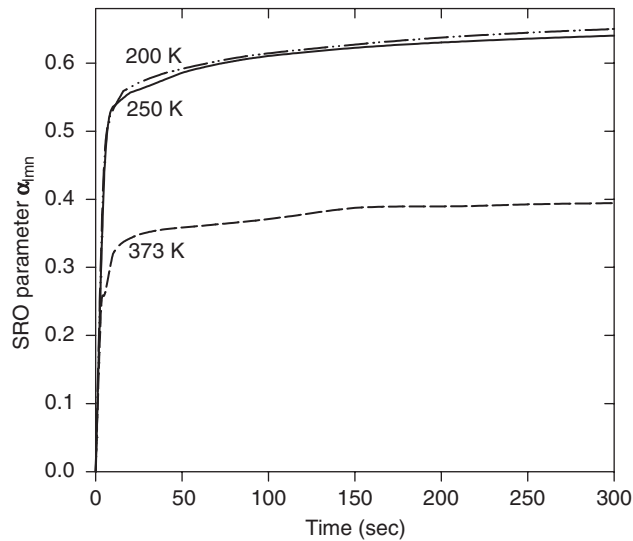


Figure 10. Time dependence of α_{110} for three different ageing temperatures. The temperature $T = 373$ K is above the coherent miscibility line.

Figure 9 shows the values of the first five SRO parameters α_{lmn} as a function of ageing time (for $T = 250$ K). The figure corresponds to the real-space images shown in figure 3. The SRO parameter shows a significant increase during the first few seconds of the ageing process. This is in agreement with the fact that already after an ageing time of $t = 5$ s for the chosen temperature ($T = 250$ K), more than 90% of all Zn atoms are parts of Zn precipitates (figure 3) and, therefore, the configuration shows a strong clustering of Zn atoms. After the first few seconds, the increase rate of α_{lmn} is reduced. Unlike the earlier growth stage, this increase in α_{lmn} is no longer caused by the formation of many new precipitates, but by the

disappearing of smaller precipitates in favour of larger precipitates (Ostwald ripening). So, the total interface area of all precipitates between the Al matrix and the Zn atoms on the surface of precipitates decreases, while the average volume of precipitates increases. In other words, the system becomes more and more an ideal phase-separating system and, therefore, the α_{lmn} values increase. Naturally, α_{110} shows the strongest increase during the first few seconds, because it is only sensitive to the first nearest neighbours and, therefore, least sensitive to the morphology of precipitates. This becomes more obvious in figure 10, which shows α_{110} for three different temperatures as a function of ageing time. The values of α_{110} for $T = 250$ K and $T = 200$ K are nearly identical. A clear change in α_{110} can only be reached if the chosen ageing temperature is above the critical temperature. As an example, figure 10 also gives the time dependence of α_{110} for $T = 373$ K ($\approx 1.1T_c$). Although the chosen parameters correspond to a point in the solid solution of the phase diagram, the alloy clearly presents a *disordered* alloy and not a *random* alloy, e.g. at $t = 100$ s, $\alpha_{110}(373 \text{ K}) \approx 0.34$ standing for a strong nearest-neighbour clustering tendency.

Following the discussion above, the slow increase of the SRO parameter after the initial formation of precipitates should lead to only a weak time dependence of α_{lmn} . Indeed, in 1989, Haeffner and Cohen [27] studied the SRO order behaviour of $\text{Al}_{0.962}\text{Zn}_{0.038}$ as a function of ageing time via x-ray diffuse scattering. The resulting experimental SRO parameters ($T = 353$ K) for two totally different ageing times are given in the second and fourth columns of table 2: Although the ageing time for sample 2 is 56 times higher (!) than for sample 1, the resulting SRO parameters for sample 2 are only 20–50% higher than those for sample 1. For a quantitative comparison, we applied our kinetic MC algorithms to an $\text{Al}_{0.962}\text{Zn}_{0.038}$ alloy and simulated ageing times of $t = 3$ h and $t = 168$ h. The simulation of an ageing time of $t = 168$ h took about five weeks CPU on a Silicon Graphics Origin 2000. The comparison is given in table 2 together with the SRO parameter of the corresponding equilibrium configuration. We see that, especially for the shorter ageing time ($t = 3$ h), the theoretical values of the first four shells are clearly larger than in experiment, while the agreement is excellent for higher shells ((222), (321), (400), etc). In principle, this observation also holds for the second sample ($t = 168$ h), although the agreement with experiment in the lower shells is better than for the first sample ($t = 3$ h). This could be a hint that our theoretical decrease in α_{lmn} is too strong at the early phase of the simulation. Other reasons could be the following: (i) The consideration of only nearest-neighbour jumps is not sufficient. (ii) The experimental values possess a large error. Nevertheless, even for the long ageing time of 168 h the configuration *cannot* be described by the equilibrium configuration. This becomes obvious by considering the SRO parameters of the equilibrium configuration given in the last column of table 2. They are nearly a factor of two higher than those for an ageing time of 168 h, emphasizing the fact that a description by thermodynamic arguments would not be sufficient.

5. Summary

We have investigated the time evolution of the precipitate size and shape distribution in Al–Zn via an atomistic quantum mechanical approach, known as ‘mixed-space cluster expansion’ [21], connected with simple kinetic MC algorithms. The change in energy between different configurations is treated exactly within the MSCE, considering all other atoms of the MC cell, but the activation barrier is simulated by the experimental diffusion constant as a function of temperature. Although this rough approximation does not allow us to describe the path of an individual Zn atom, it should be a very good approximation for the description of the time evolution of the precipitate distribution. We find that: (i) The growth of Zn precipitates in Al-rich Al–Zn alloys follows, after the first few seconds, a $d_m \propto t^{1/3}$ power law

Table 2. Experimental SRO parameters of an $\text{Al}_{0.962}\text{Zn}_{0.038}$ alloy given by Haeffner and Cohen [27] at $T = 353$ K for $t = 3$ h and $t = 168$ h and comparison to kinetic MC values (this work). The right column gives the calculated parameters for the corresponding equilibrium configuration.

(<i>lmn</i>)	$\alpha_{lmn}^{\text{exp}}$ ($t = 3$ h)	$\alpha_{lmn}^{\text{theo}}$ ($t = 3$ h)	$\alpha_{lmn}^{\text{exp}}$ ($t = 168$ h)	$\alpha_{lmn}^{\text{theo}}$ ($t = 168$ h)	$\alpha_{lmn}^{\text{theo}}$ (equil.)
000	0.967	1.000	1.113	1.000	1.000
110	0.176	0.309	0.244	0.357	0.569
200	0.110	0.282	0.154	0.296	0.512
211	0.094	0.184	0.141	0.231	0.473
220	0.086	0.154	0.125	0.198	0.449
310	0.077	0.114	0.105	0.168	0.422
222	0.072	0.100	0.099	0.133	0.389
321	0.070	0.074	0.090	0.122	0.377
400	0.053	0.077	0.070	0.103	0.368
330	0.048	0.051	0.076	0.090	0.347
411	0.058	0.057	0.072	0.091	0.351
420	0.054	0.047	0.070	0.080	0.336

and, therefore, represents an example of classical Ostwald ripening. (ii) The distribution of precipitates shows a temperature dependence: the higher the ageing temperature, the smaller the distribution width. (iii) The SRO parameters show a dramatic increase during the first few seconds of the ageing process caused by the formation of precipitates. Compared to this initial increase of the α_{lmn} values, the increase caused by the following change in the distribution by Ostwald ripening is weak. Nevertheless, our quantitative comparison between experimental and theoretical SRO parameters shows that even after an ageing time of $t = 168$ h, it is not possible to describe the corresponding structure by use of the equilibrium structure: the found SRO parameters are up to a factor of two smaller than those corresponding to the equilibrium configuration.

Acknowledgments

The work at NREL was supported by the Office of Science, Basic Energy Science, Material Science Division, Condensed Matter Theory, US Department of Energy under Contract No DE-AC36-99-GO10337.

References

- [1] Guinier A 1959 *Solid State Phys.* **9** 293
- [2] Müller S, Wang L-W, Zunger A and Wolverton C 1999 *Phys. Rev. B* **60** 16448
- [3] Massalski T B 1986 *Binary Alloy Phase Diagram* ed J L Murray, L H Bennett and H Baker (Ohio: American Society of Metals)
- [4] Hatch J E 1998 *Aluminum: Properties and Physical Metallurgy* (Ohio: American Society of Metals)
- [5] Cohen J B 1986 *Solid State Phys.* **39** 131
- [6] Khachaturyan A G 1983 *Theory of Structural Transformations in Solids* (New York: Wiley)
- [7] Müller S, Wolverton C, Wang L-W and Zunger A 2000 *Acta Mater.* **48** 4007
- [8] Müller S, Wolverton C, Wang L-W and Zunger A 2001 *Europhys. Lett.* **55** 33
- [9] Voter A F 1986 *Phys. Rev. B* **34** 6819
- [10] Fichtorn K A and Weinberg W H 1991 *J. Chem. Phys.* **95** 1090
- [11] Börtz A B, Kalos M H and Lebowitz J L 1975 *J. Comp. Phys.* **17** 10
- [12] Jacobsen J, Jacobsen K W, Stoltze P and Norskov J K 1995 *Phys. Rev. Lett.* **74** 2295

- [13] Wang Y, Chen L-Q and Khachaturyan A G 1991 *Scripta Metall.* **25** 1387
- [14] Chan L-Q and Khachaturyan A G 1992 *Phys. Rev. B* **46** 5899
- [15] Wang Y, Chen L-Q and Khachaturyan A G 1993 *Acta Metall.* **41** 279
- [16] Dobretsov V Y, Vaks V G and Martin G 1996 *Phys. Rev. B* **54** 3227
- [17] Rubin G and Khachaturyan A G 1999 *Acta Mater.* **47** 1995
- [18] Lee J K 1997 *Mater. Sci. Eng. A* **238** 1
- [19] Choy J-H and Lee J K 2000 *Mater. Sci. Eng. A* **285** 195
- [20] Lee J K 1996 *Metall. Mater. Trans.* **27A** 1449
- [21] Zunger A 1994 *NATO ASI on Statics and Dynamics of Alloy Phase Transformations* ed P E A Turchi and A Gonis (New York: Plenum) p 361
- [22] Ceperley D M and Alder B J 1980 *Phys. Rev. Lett.* **45** 567
- [23] Perdew J P and Zunger A 1981 *Phys. Rev. B* **23** 5048
- [24] Wolverton C 1999 *Phil. Mag. Lett.* **79** 683
- [25] Wolverton C 2000 *Model. Simul. Mater. Sci.* **8** 323
- [26] Ramlau R and Löffler H 1983 *Phys. Status Solidi a* **79** 141
- [27] Haeffner D R and Cohen J B 1989 *Acta. Metall.* **37** 2185
- [28] Laks D B, Ferreira L G, Froyen S and Zunger A 1992 *Phys. Rev. B* **46** 12587
- [29] Ihm J, Zunger A and Cohen M L 1979 *J. Phys. C* **12** 4409
- [30] Swendson R H and Wang J-S 1987 *Phys. Rev. Lett.* **58** 86
- [31] Wolff U 1989 *Phys. Rev. Lett.* **62** 361
- [32] Lu Z W, Laks D B, Wei S-H and Zunger A 1994 *Phys. Rev. B* **50** 6642
- [33] Soisson F, Barbu A and Martin G 1996 *Acta Mater.* **44** 3789